AGU PUBLICATIONS

JGR

Journal of Geophysical Research: Oceans

RESEARCH ARTICLE

10.1002/2016JC012633

Special Section:
Dense Water Formations in the North Western Mediterranean: From the Physical Forcings to the Biogeochemical Consequences

Characterization of Convective Plumes Associated With Oceanic Deep Convection in the Northwestern Mediterranean From High-Resolution In Situ Data Collected by Gliders

Félix Margirier[1], Anthony Bosse[1,2], Pierre Testor[1], Blandine L'Hévéder[1], Laurent Mortier[1,3], and David Smeed[4]

[1]Sorbonne Universités (UPMC, Univ Paris06)-CNRS-IRD-MNHN, Laboratoire LOCEAN, Paris, France, [2]Geophysical Institute, University of Bergen, Bergen, Norway, [3]ENSTA ParisTech, Palaiseau, France, [4]National Oceanography Centre, Southampton, UK

Key Points:
- From a glider flight model, we extract for the first time the statistical physical and biogeochemical characteristics of convective plumes
- Intense vertical velocities are observed (up to 18 cm s^{-1}) and the plumes are found to cover about one third of the deep convection area
- Vertical velocities scaled by atmospheric fluxes inducing downward buoyancy fluxes with a vertical diffusion coefficient of 10 m^2 s^{-1}

Correspondence to:
F. Margirier,
felix.margirier@locean-ipsl.upmc.fr

Citation:
Margirier, F., Bosse, A., Testor, P., L'Hévéder, B., Mortier, L., & Smeed, D. (2017). Characterization of convective plumes associated with oceanic deep convection in the northwestern Mediterranean from high-resolution in situ data collected by gliders. *Journal of Geophysical Research: Oceans, 122*, 9814–9826. https://doi.org/10.1002/2016JC012633

Received 15 DEC 2016
Accepted 28 SEP 2017
Accepted article online 6 OCT 2017
Published online 13 DEC 2017

Abstract Numerous gliders have been deployed in the Gulf of Lions (northwestern Mediterranean Sea) and in particular during episodes of open-ocean deep convection in the winter 2012–2013. The data collected represents an unprecedented density of in situ observations providing a first in situ statistical and 3-D characterization of the important mixing agents of the deep convection phenomenon, the so-called plumes. A methodology based on a glider-static flight model was applied to infer the oceanic vertical velocity signal from the glider navigation data. We demonstrate that during the active phase of mixing, the gliders underwent significant oceanic vertical velocities up to 18 cm s^{-1}. Focusing on the data collected by two gliders during the 2012–2013 winter, 120 small-scale convective downward plumes were detected with a mean radius of 350 m and separated by about 2 km. We estimate that the plumes cover 27% of the convection area. Gliders detected downward velocities with a magnitude larger than that of the upward ones (−6 versus +2 cm s^{-1} on average). Along-track recordings of temperature and salinity as well as biogeochemical properties (dissolved oxygen, fluorescence, and turbidity) allow a statistical characterization of the water masses' properties in the plumes' core with respect to the "background": the average downward signal is of colder (-1.8×10^{-3} °C), slightly saltier ($+4.9 \times 10^{-4}$ psu) and thus denser waters ($+7.5 \times 10^{-4}$ kg m^{-3}). The plunging waters are also on average more fluorescent ($+2.3 \times 10^{-2}$ μg L^{-1}). The plumes are associated with a vertical diffusion coefficient of 7.0 m^2 s^{-1} and their vertical velocity variance scales with the ratio of the buoyancy loss over the Coriolis parameter to the power 0.86.

1. Introduction

The deep convection phenomenon occurs in winter in the northwestern Mediterranean Sea and renews the deep waters by ventilating them. The volume of the newly formed deep waters depends both on the oceanic preconditioning and on air-sea fluxes inducing buoyancy losses at the surface. The Gulf of Lions is regularly subject to subsequent atmospheric forcings under the intense cold winds Tramontane and Mistral. In winter, those winds induce strong evaporation and an intense cooling of surface waters (∼−1,000 W m^{-2}; Leaman & Schott, 1991) and are responsible for buoyancy losses and vertical deep mixing. On the other hand, the horizontal circulation in the northwestern Mediterranean Sea controls heat and mass transfers and thus is a key to the ocean preconditioning of the deep convection events occurring in the Gulf of Lions, modulating in time and space the capacity of atmospheric forcing to trigger deep mixing (Grignon et al., 2010; Mertens & Schott, 1998).

Documented for the first time by the pioneer MEDOC Group in 1970 (MEDOC Group, 1970) and centered around 42°N, 5°E (on the Rhône deep sea fan), the processes involved in deep convection can be cut down into three phases (Marshall & Schott, 1999) that may overlap.

1.1. Hydrological Preconditioning

The convection event depends on the preconditioning which is variable over years as it depends on the hydrographic structure of the water column. The cyclonic circulation in the northwestern Mediterranean induces a doming of the isopycnals exposing sparsely stratified waters to the atmospheric forcing in the center of the gyre. The deep waters are thus nearer to the surface and easier to grasp for a local

cooling/evaporation. Furthermore, the surface Atlantic Waters (AW) mix with warm and more particularly salty Levantine Intermediate Waters (LIW) lying below in the process, which can increase the efficiency of the mixing.

1.2. Vertical Mixing

The intense atmospheric forcing cools the surface waters and destabilizes the water column, especially in the preconditioned areas where plumes form when the mixing reaches great depths. According to the theory, their typical size is of 1 km in diameter over the whole mixed layer and the vertical velocities in those plumes can reach up to 10 cm s^{-1} (Leaman & Schott, 1991; Visbeck et al., 1996). This vision is only partial though, the mixed patch being variable both in size and depth from year to year and previously observed only from ADCP's on moorings at certain depths and only sampling plumes crossing the mooring lines. All the scales are at stake (Marshall & Schott, 1999, Figure 4) with plumes, eddies, and the gyre circulation interacting.

Both numerical and turning table experiments conducted by Maxworthy and Narimousas (1994)—see review by Marshall and Schott (1999)—indicate that the baroclinic instability exports new waters out of the mixed patch which can contribute to a slowing of the mixing as such. However, MEDOC Group (1970) suggested that this baroclinic instability could have a feedback on the ocean-atmosphere surface fluxes by bringing waters to the surface and maintaining the mixing. This is verified by numerical simulations which show that the combination of the atmospheric forcing and the baroclinic instability is responsible for the vertical mixing and is more powerful combined than taken separately (Legg & McWilliams, 2001; Straneo & Kawase, 1999). This demonstrates the dual role of the baroclinic instability and Visbeck et al. (1996) suggest a mixed-layer depth resulting from an equilibrium between the baroclinic instability and the forcing.

1.3. Lateral Exchanges and Spreading

After the intense forcing episodes, lateral energy transfers take over and eddies form. They spread due to the effects of stratification and rotation. Schott et al. (1996) observed fluctuations in temperature with a mooring placed along the Spanish coast, which could imply an incorporation of these waters to the northern current flowing along the continental slope north and west of the convection area. They estimated that 50% of the newly formed waters could escape with the current. Madec et al. (1991) numerical simulations hypothesized this mechanism while Testor & Gascard (2006) estimated that 50% of the newly formed waters spread in the basin in coherent (lifespan over 1.5 years) lenticular (thickness h $\sim$ 1 km) submesoscale eddies (5–10 km in radius).

During winter 2012–2013, open-ocean deep convection occurred in the Gulf of Lions (northwestern Mediterranean Sea) and has been thoroughly documented thanks in particular to the simultaneous deployment of several gliders, of Argo profiling floats, dedicated ship cruises, and a mooring located within the mixed patch (Testor et al., 2017). Because of the difficulty to conduct a cruise in winter due to strong weather events (Eriksen & Rhines, 2008), gliders are of crucial importance to observe oceanic processes such as deep convection. The surface of the mixed patch has been estimated to be 15,500 km^2, corresponding to a formation of 1.1 Sv of deep waters in 2012 (Durrieu de Madron et al., 2013) and 2 Sv in 2013 when up to five gliders were at sea simultaneously covering the area in a synoptic way (Bosse, 2015).

We compute water vertical velocities from a glider flight model to assess the vertical velocities associated with intense deep convection episodes in the Gulf of Lions in the winter 2012–2013 in section 2. Section 3 presents the derived method to detect convective plumes and to give a description of their properties relative to surrounding waters. We finally assess the plume coverage of the convective region and confirm the effect of rotation on the plume characteristics in section 4.

2. Materials and Methods

2.1. Description of the Data Set and Methodology

2.1.1. Data

The gliders data collected during the 2012–2013 winter provides an unprecedented density of in situ observations during an event of open-ocean deep convection. Gliders move along saw-tooth trajectories between the surface and a maximum depth of 1,000 m, covering a distance of 2–4 km in a time period of 2–4 h between two surfacings. They record temperature and salinity as well as biogeochemical properties

(dissolved oxygen, chlorophyll-a fluorescence, turbidity-optodes Anderaa, and Wet-Lab ecopuck FLNTU) along their trajectory. During the active phase of mixing of the deep convection, the gliders have undergone significant oceanic vertical upward and downward velocities, stronger than 10 cm s^{-1}, that could be seen by just looking at the pressure time series of the gliders. With a vertical speed of 10–25 cm s^{-1} relative to the water, gliders present trajectories that were significantly perturbed by the oceanic vertical velocities associated with the plumes. The gliders were equipped with an unpumped CTD probe (SBE-41) that generally needs to be corrected with an offset as a first order correction for each single deployment. The SBE-41 CTD sensor has an absolute accuracy of 0.002°C and 0.003 psu, and relative accuracies of 0.0001°C and 0.0007 psu. As in Bosse et al. (2016) and in Testor et al. (2017), we compared gliders data with nearby calibrated CTD casts from R/Vs (<15 km and <3 days), and with the calibrated mooring lines LION and DYFAMED (<2.5 km and <18 h, about the inertial period in this region). The cross-platform hydrographical consistency was checked in the deeper layers sampled by the gliders (700–1,000 m) because the T/S variability is relatively small at those depths. The deduced T and S offsets are of 0.001°C and of −0.003 psu for the deployment Campe/ASICSMED and of 0.001°C and of 0.01 psu for the deployment Milou/ASICSMED. This study focuses on statistical relative differences and the results are thus not affected by the applied offsets. In addition, the thermal lag issue of the unpumped CTD probe that can affect salinity measurements in strong thermoclines (order of 1–10°C over less than 10 m) has been corrected following Garau et al. (2011). Those are second-order corrections because there is no strong thermocline in the homogeneous convection area where the plumes are observed.

2.1.2. Glider-Static Flight Model

To go further and get quantitative water vertical velocities, a methodology based on a glider quasi-static flight model is applied to infer the oceanic vertical velocity signal from the glider navigation data, following the methods in Merckelbach et al. (2010) and Frajka-Williams et al. (2011). The glider is modeled in a quasi-steady flight and in the absence of vertical displacements. Thus, the vertical velocity of the water can be extracted from the gliders vertical movement, giving an estimate of the convective velocities.

The different forces exerted on the glider, represented in Figure 1, follow the ensuing equations (the definitions of the different variables are given in Table 1),

$$F_B = g\rho(V_g(1-\epsilon P+\alpha_T(T-T_0))+\triangle V_g), \tag{1}$$

$$F_g = m_g g, \tag{2}$$

$$F_L = \frac{1}{2}\rho S U^2 a\alpha, \tag{3}$$

$$F_d = \frac{1}{2}\rho S U^2 (C_{D_0}+C_{D_1}\alpha^2). \tag{4}$$

The projections of the glider-static equilibrium on the vertical and horizontal thus give,

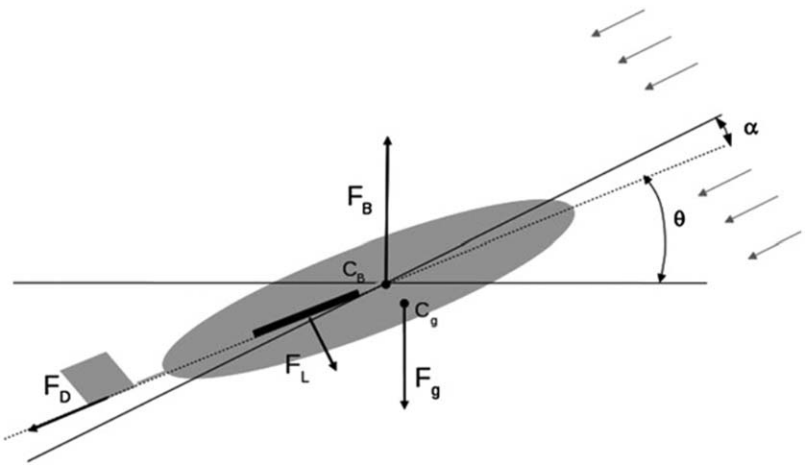

Figure 1. Schematic view of a glider flight on a vertical plane: Buoyancy force F_B, gravity F_g, lift F_L, and drag F_D; the sum of attack angle α and pitch θ makes the glide angle γ (from L'Hévéder et al., 2013).

Table 1
Parameters of the Glider Flight, Their Origins and Their Typical Value During an Ascent or a Descent

Parameter	Description	Origin	Typical value	Unit
F_B	Buoyancy force	Computed		N
F_g	Gravitational force	Computed		N
F_L	Lift force	Computed		N
F_d	Drag force	Computed		N
U	Glider velocity	Computed	0.4	$m\ s^{-1}$
u_{glider}	Glider horizontal velocity	Computed		$m\ s^{-1}$
w_{glider}	Glider vertical velocity	Computed		$m\ s^{-1}$
w_{water}	Water vertical velocity	Computed		$m\ s^{-1}$
α	Attack angle	Computed	$\pm$2–3	°
γ	Glide angle	Computed	$\pm$25	°
θ	Pitch angle	Measured by glider sensors	$\pm$22	°
P	Water pressure	Measured by glider sensors		Pa
T	Water temperature	Measured by glider sensors		°C
ρ	Water density	Measured by glider sensors		$kg\ m^{-3}$
C_{D_0}	Parasite drag	Optimized	0.1	rad^{-2}
ϵ	Hull compressibility	Optimized	5.7×10^{-10}	Pa^{-1}
V_g	Glider volume	Optimized	55.5	L
T_0	Reference water temperature	Constant	13.1	°C
g	Acceleration of gravity	Constant	9.81	$m\ s^{-2}$
m_g	Glider mass	Characteristic of the glider	57	kg
$\triangle V_g$	Pumped volume	Characteristic of the glider	0.25	L
S	Wing surface area	Characteristic of the glider	0.1	m^2
C_{D_1}	Induced drag	Characteristic of the glider	2.88	rad^{-2}
a	Lift coefficient	Characteristic of the glider	6.1	rad^{-1}
α_T	Thermal expansion coefficient	Characteristic of the glider	7.05×10^{-5}	K^{-1}

$$/z : F_B - cos(\gamma)F_L - sin(\gamma)F_d - F_g = 0, \tag{5}$$

$$/x : cos(\gamma)F_d - sin(\gamma)F_L = 0. \tag{6}$$

The water's vertical velocity is estimated as the difference between the velocity derived from the rate of change of pressure and that predicted by the glider flight model.

$$w_{water} = \frac{dz_P}{dt} - w_{glider}. \tag{7}$$

In a quasi-static equilibrium, injecting equations (3) and (4) in the projection (equation (6)) of the equilibrium and considering that $\alpha + \theta = \gamma$ gives the following expression for the angle of attack α:

$$\alpha = \frac{C_{D_0} + C_{D_1}\alpha^2}{atan(\theta + \alpha)}. \tag{8}$$

In order to compute the water vertical displacements with precision, some parameters are optimized (see Table 1) with the following cost function:

$$J(C_{D_0}, \epsilon, V_g) = \sum \left(\frac{dz_P}{dt} - w_{glider} \right)^2. \tag{9}$$

Vertical movements of the water are minimized (the model makes the hypothesis there are none) over a 24 h period (long enough to consider that the mean vertical velocities are null). We are thus able to compute α from equation (8) and thus U (substituting equations (1)–(4) into equation (6)). We then obtain the glider's velocity components,

$$u_{glider} = Ucos(\theta + \alpha), \tag{10}$$

$$w_{glider} = Usin(\theta + \alpha). \tag{11}$$

And we then finally retrieve w_{water} from equation (7).

2.2. Validation of the Resulting Water Velocity

Figure 2 portrays the evolution of the resulting vertical water velocity in the absence and in the presence of a convection episode. The optimization algorithm converges and the parameters obtained by this method vary slightly: 10% of their values for C_{D_0} and ϵ, and the variation of the glider volume (10 cc) is negligible compared to its volume V_g (55,000 cc). Furthermore, the robustness of the method is highlighted by the fact that the extracted vertical velocities are not affected by the glider vertical movement (plunging or ascending). This is verified in Figure 2a: at 08:00 the glider, undergoing large water vertical velocities (larger than 5 cm s^{-1}), switches from a downcast to an upward motion and the water vertical velocity remains coherent during the change.

To assess the quality of our results, we compared the vertical water velocities computed with the glider data to the ones measured at the LION mooring line situated in the middle of the mixed patch at 42°02′N, 4°41′E and a bottom depth at 2,350 m (Houpert et al., 2016; Testor et al., 2016)—current meters moored at 150, 250, 500, and 1,000 m depths are used as the one at 2,315 m allows no comparison with the glider data. Figure 3 provides a comparison of those water vertical velocities. The glider data reproduce very well the distribution of vertical displacements both during convective episodes and in their absence. The 30-min sampling rate of the LION mooring's current meters does not allow more than two or three points inside a plume but does enable a statistical comparison with the gliders' data. Noticing that the velocities are never greater than 3–4 cm s^{-1} in the absence of convection, we thus used it to define a threshold for the detection of convective episodes: a convective episode is detected when 10% of the velocities are greater than 4 cm s^{-1} over a 24 h period. This enables an automatic detection of convective episodes, which are then cut down into convective plumes defined by both those velocities and a lateral extension over 100 m. We

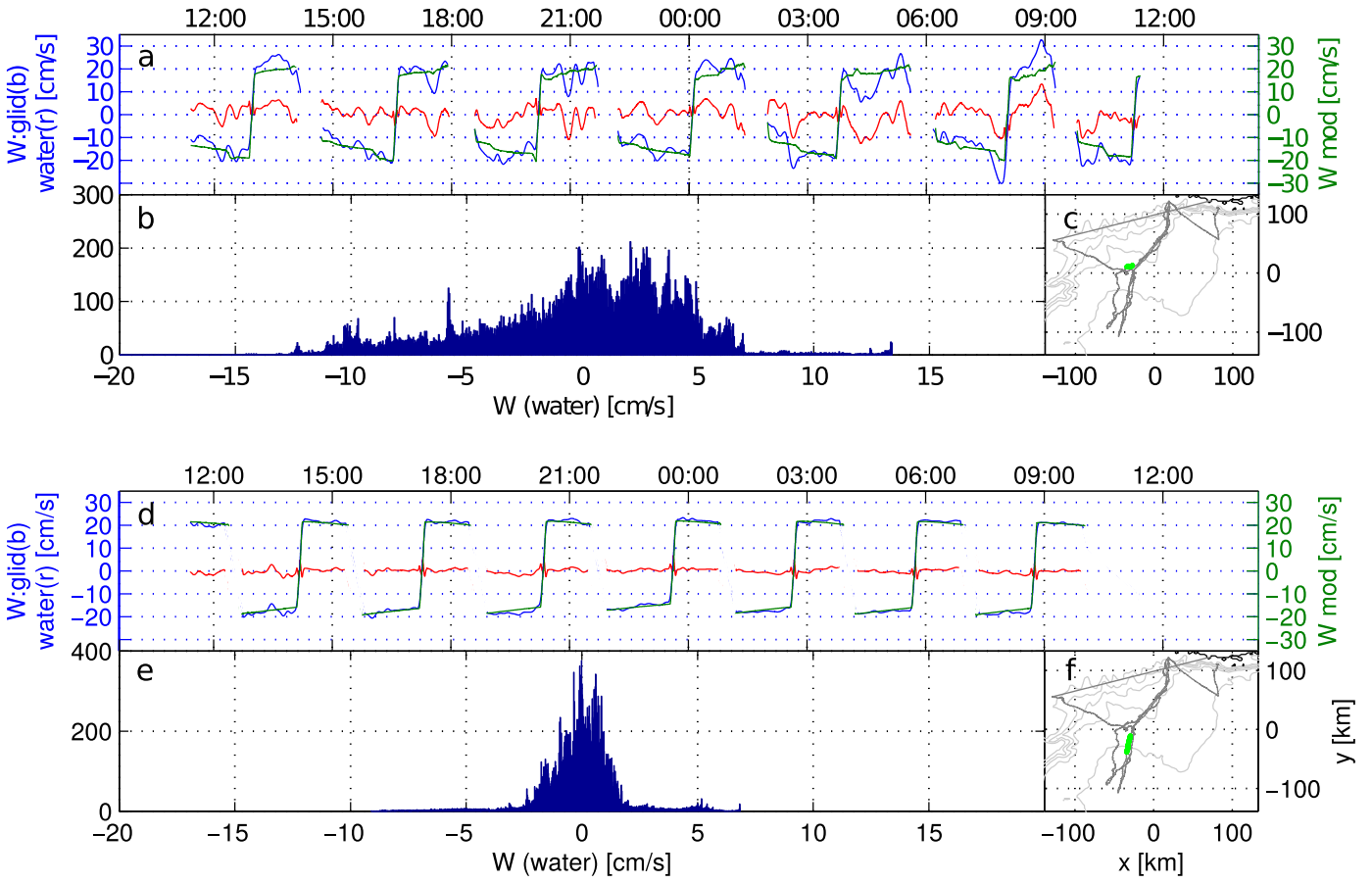

Figure 2. Flight parameters and resulting water vertical velocity in the absence of convection the 30 January 2013 (bottom) and during convection the 23 February 2013 (top). (a) Glider vertical velocity w_{glider} (blue), pressure gradient induced velocity $\frac{dZ_P}{dt}$ (green), and water vertical velocity w_{water} (red). (b) Distribution of water vertical velocities. (c) Glider trajectory, in green the portion represented above. (d) Glider vertical velocity w_{glider} (blue), pressure gradient induced velocity $\frac{dZ_P}{dt}$ (green), and water vertical velocity w_{water} (red). (e) Distribution of water vertical velocities. (f) Glider trajectory, in green the portion represented above.

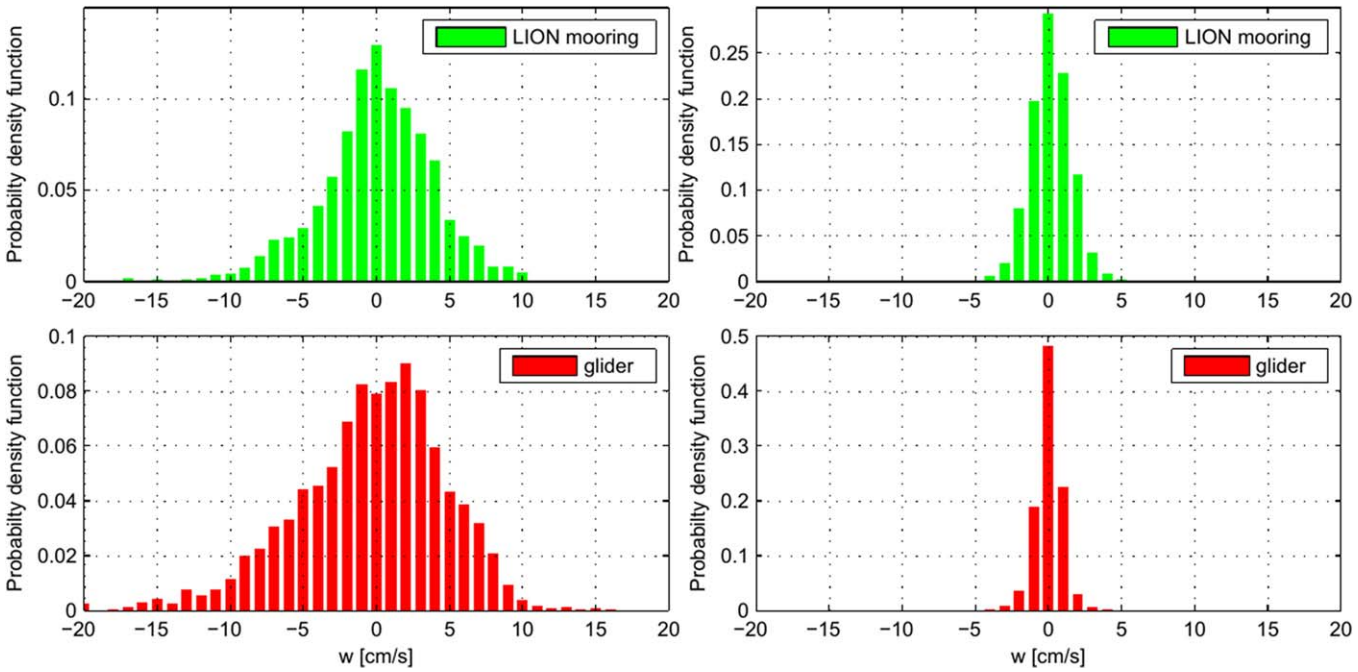

Figure 3. Velocities distribution over the first 1,000 m on the LION mooring (up) and measured by the glider (bottom) from 1 February 2013 to 15 March 2013. (left) During periods of high buoyancy loss (net heat fluxes <-500 W m^{-2}); (right) during low buoyancy loss (net heat fluxes >-100 W m^{-2}) episodes.

thus exclude the plumes for which only the border is sampled by imposing a minimum distance of 100 m during which the glider is exposed to those significant downwelling velocities. This enables the detection of 120 plumes over the two deployments Campe/ASICSMED and Milou/ASICSMED which were at sea during the intense convective winter of 2012–2013.

3. Characterization of Convective Plumes

The properties measured by glider Campe are represented in Figure 5. The glider performed north-south transects across the Gulf of Lions as can be seen in Figure 4 where the tracks of gliders Campe/ASICSMED and Milou/ASICSMED are shown. In Figure 5, one can notice the intense fronts of the northern current and the North Balearic front surrounding the mixed patch. During those transects, glider trajectories are not straight lines as we usually expect because of the strong vertical velocities associated with plumes deviating it. Figure 5 highlights various small-scale ($<$1 km) features associated with temperature, salinity, and density variations and questions the idea of a homogeneous mixed patch.

We also note that the waters are already homogeneous during the gliders' first passage in the Gulf of Lions (27 January to 3 February), indicating a previous mixing episode. No significant vertical velocities are detected during the first transect. The heat fluxes (retrieved from ALDERA reanalysis and interpolated along the glider track) are weak, inducing no buoyancy losses and thus no plumes at that time.

Later on, we detect two main episodes of convection (8–11 February and 24–27 February) where vertical velocities are large and the water is homogeneous over depths. Significant heat losses (consistently over $-1{,}000$ W m^{-2}) at the surface of the sea are followed by strong vertical velocities and active mixing. It is also noted that the waters get denser, colder, and richer in oxygen over time due to the mixing process.

If the glider was under vertical inertial movements, it would be associated with the Brunt-Väïsälä frequency $N \sim \frac{2*\Pi}{3600}$ (time scale of 1 h) but the stratification is a lot smaller in the mixed patch and N yields a period of 4–8 h. The plume persistence time scale is estimated to scale in f^{-1} by Marshall and Schott (1999), giving 17 h. Sea state varies on a scale of 4 h as a result of the variability of the atmospheric forcing, so considering the glider crosses a plume in 1–2 h, we can thus extract a typical convective plume (see Figure 6) to get its properties. Inside the plume core, the downwelling waters are colder and saltier, thus denser. The downwelling velocities are also greater than the upwelling ones around our structure. Some signatures also appear

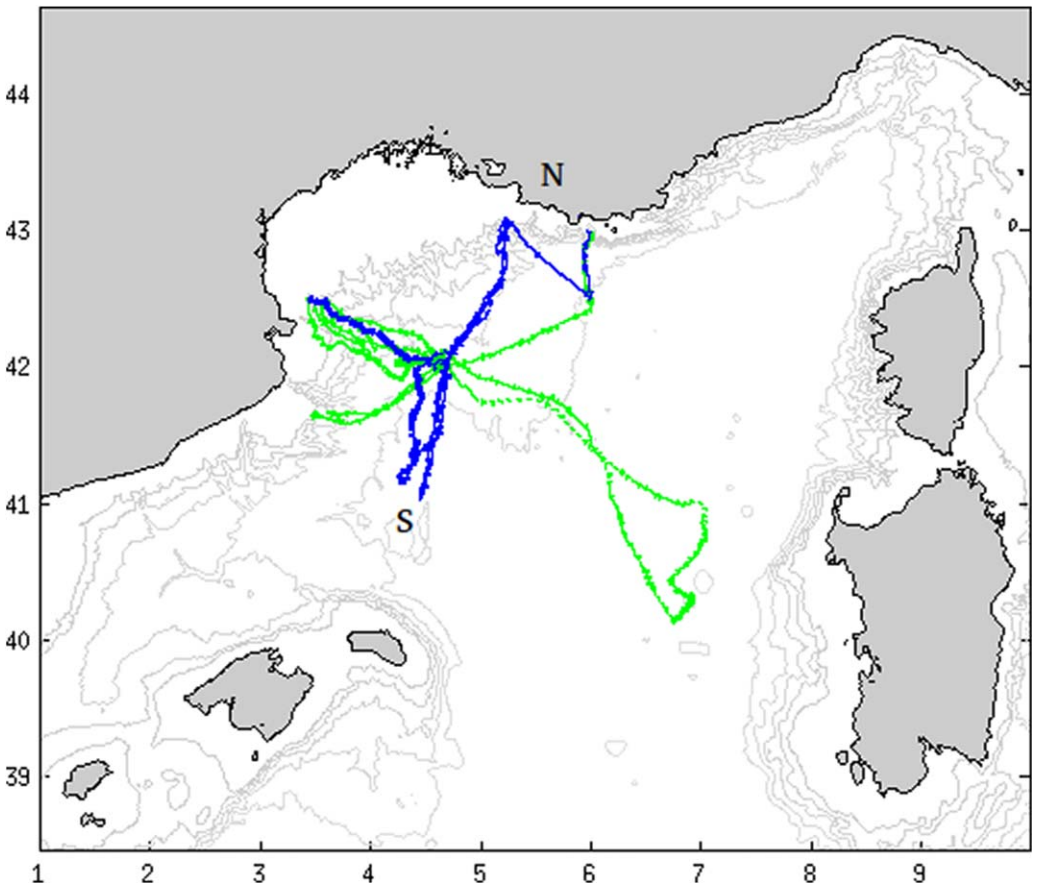

Figure 4. Milou/ASICSMED (green) and Campe/ASICSMED (blue) glider tracks. N (for North) and S (for South) are geographical markers for the transect used in Figure 5.

for the biogeochemical parameters, but not as clearly (oxygen is plotted relative to a trend estimated on a downcast/upcast).

In order to confirm those tendencies and generalize, we normalize the 120 detected plumes. To do this, we associate each plume to its radius (half of the distance where velocities are negative) and plot the set of data at a relative distance to the center of the structure (folding the plume around its center). The normalized folded plumes are superimposed in Figure 7. The running mean of those normalized plumes is performed on the points within the standard deviation after the exclusion of outliers (5th and 95th percentiles considering a Gaussian distribution). Negative velocities (-6 cm s^{-1}) are three times larger than positive ones (around $+2$ cm s^{-1}). The physical and biogeochemical properties of the plumes are plotted compared to their value at R = 1 where the vertical velocities are null. Their signatures are then retrieved statistically as the difference between the mean value far from the plume at $R = 2.5$ compared to that in the center of the plumes at $R = 0$. The temperature, salinity, density, and fluorescence panels in Figure 7 present a plateau in the core of the plume ($R < 0.4$) suggesting a coherent structure. The gray shading being the running standard deviation, the running standard error on the mean is then retrieved dividing by the square root of the number of points in the running bins and is very small due to the large number of points in each bin (minimum 1,363 points per bin). Statistically, the downwelling waters appear colder ($-1.81\pm0.04\times10^{-3}$ °C), slightly saltier ($+4.9\pm0.3\times10^{-4}$ psu) and thus denser ($+7.5\pm0.3\times10^{-4}$ kg m^{-3}). The results for the temperature are one order of magnitude greater than the accuracy of the sensor for the temperature (1×10^{-4} °C) and for the salinity, the results are of the order of magnitude of the sensor resolution (7×10^{-4} psu), the results being statistically significant due to the large number of plumes observed. They are also on average moderately more fluorescent (phytoplankton being dragged down, $+2.30\pm0.03 \times10^{-2}$ μg L^{-1}). Although no signal can be directly retrieved from the oxygen and turbidity panels, it is worth noting that individual plumes have small signatures in turbidity of different signs which may

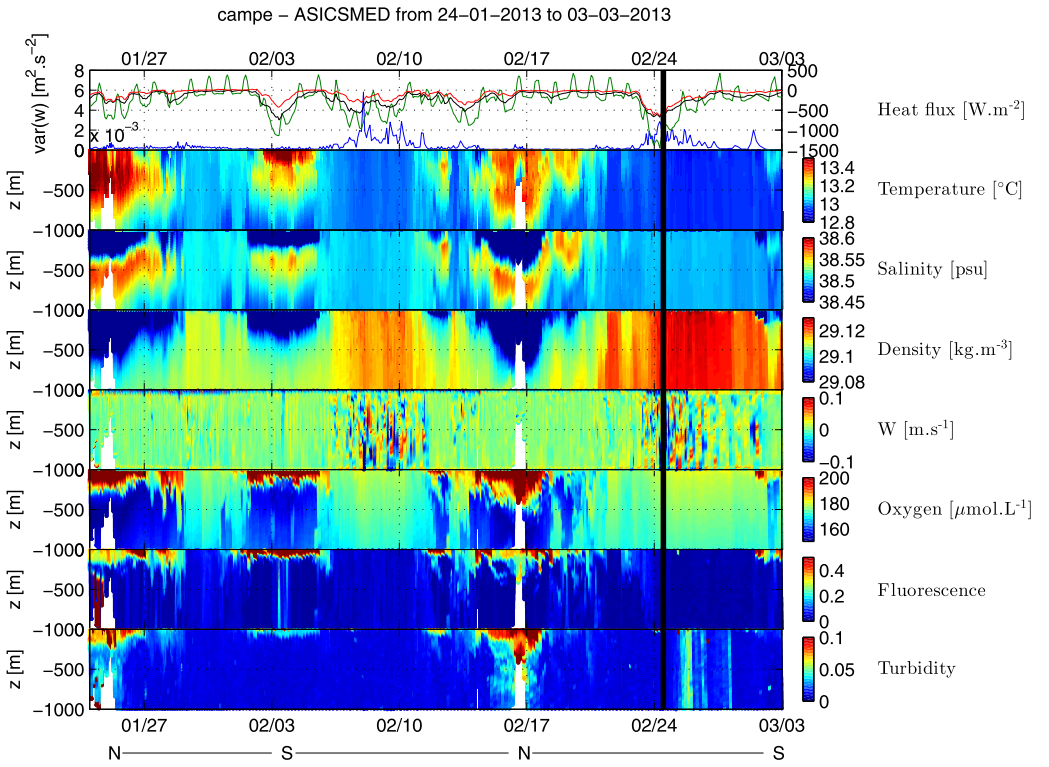

Figure 5. Glider transect Campe/ASICSMED. For the top figure, the variance of the vertical velocities during a yo (a downcast and an upcast) is represented in blue and the sensible, latent, and net heat fluxes are, respectively, in red, black, and green. The black vertical line corresponds to the plume represented in Figure 6. Two convective episodes of approximately three days are seen following important buoyancy losses due to the heat fluxes: 8–11 and 24–27 February. N and S letters represent the northern and southern outreaches of the glider (see Figure 4).

compensate overall, some show more turbid and oxygenated plunging waters while others have the opposite downwelling signature (not shown here). In general, the relatively small differences detected between the core of the plumes and their environment reflect the fact that the gliders evolve in an already well mixed area.

We assess the plumes' vertical structure by binning the collected data by the depth where the glider crossed the maximum vertical velocity of the plume. By doing so, we sort the plumes by depth of maximum velocity and are thus able to suggest a vertical structure of convective plumes. As the mixed layer reached the bottom during the mixing episodes (Houpert et al., 2016), the deceleration when reaching the bottom cannot be well represented here as the gliders did not fly deeper than 1,000 m. We observe that the vertical velocities in the plumes are somewhat larger when the plumes are detected deeper and that they seem to get wider as they descend, similarly to atmospheric convection.

4. Discussion

4.1. Spatial Coverage

In order to complete the study of plumes, we have to take into account that the glider crosses the plumes neither necessarily in its center nor horizontally. The vertical extension of a plume crossing has been found to vary from 200 m up to the whole extent of a descent/ascent: 1,000 m. The horizontal mean radius of the detected plumes is of 312 m. This is in good agreement with Marshall and Schott (1999) who predicted a typical lateral extension of 500 m. We consider a simple isotropic cylindrical model for the plumes and with the hypothesis that the glider can cross a plume any given way. Taking into account the 100 m threshold established previously for the detection, we find an effective plume radius of 350 m and a mean distance of 1.85 km in between plumes along a glider track. This is in good agreement with previous estimates made by Merckelbach and Smeed (2006) and Smeed et al. (2007) (R ∼300 m and 2 km between plumes) and

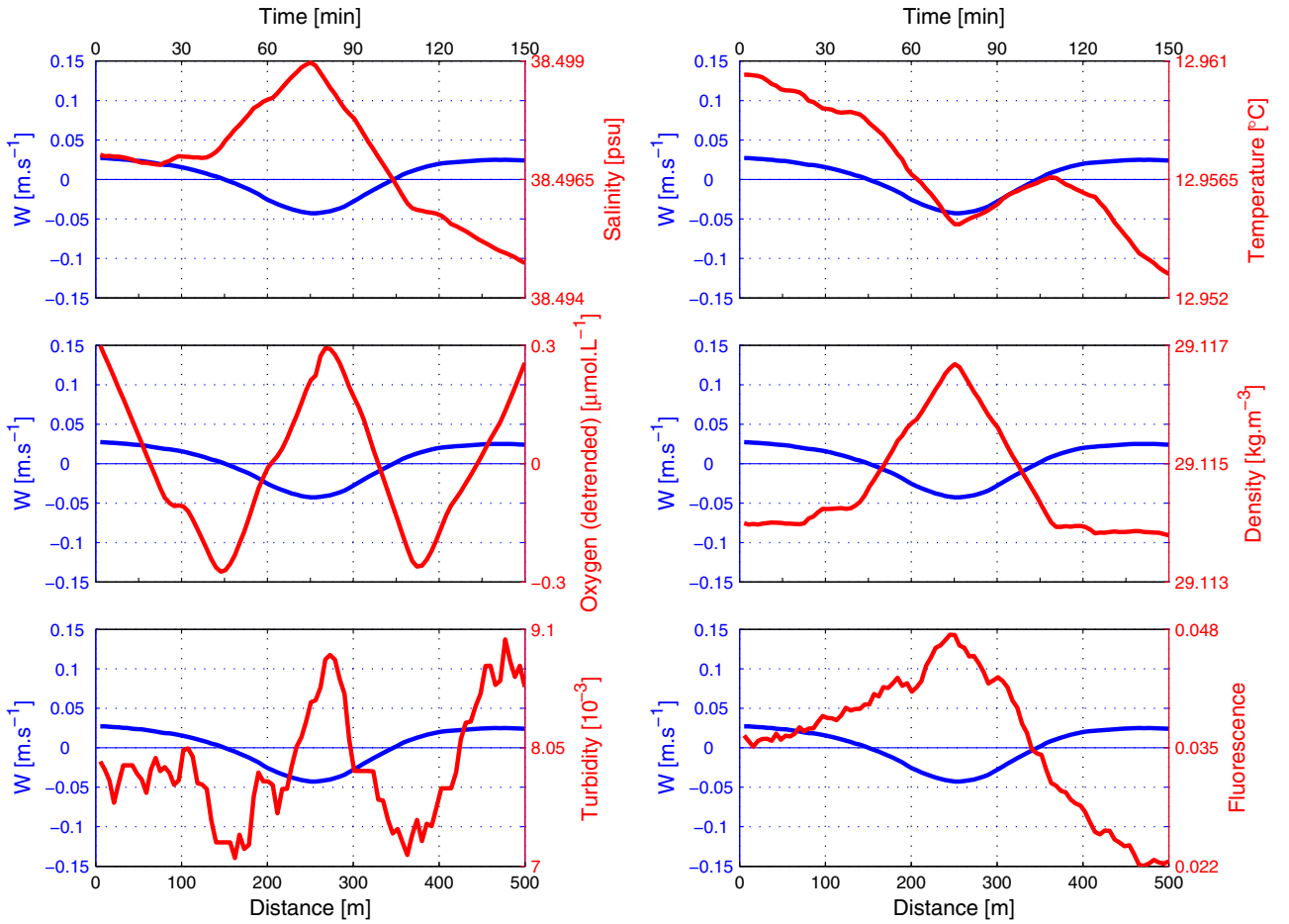

Figure 6. A typical convective plume (marked in time by a black vertical in Figure 5). Top left to bottom right: Salinity, temperature, oxygen (detrended); density, turbidity, and fluorescence (in red); water vertical velocity (in blue).

Paluszkiewicz et al. (1994, R ~300–500 m). Computing the mean distance between plumes along the glider track, we find that plumes cover 40% of the trajectory and considering an isotropic distribution of the plumes on a triangular horizontal grid with those distance characteristics gives a 27% coverage of the convective patch by negative velocities, while the rest is covered by positive and generally small velocities as suggested by Send and Marshall (1995). This simple coverage scheme and the associated velocity coverage of the area gives a 91% correspondence between the upwelling and downwelling waters, also allowing for lateral spreading at depth. The knowledge of the small structures in the convective patch could allow a better parametrization of this key phenomenon renewing deep waters in models. Ocean general circulation models see convection as a subgrid phenomenon and the physics of mixing are parametrized in order to render the distribution of heat and the mixing. Some LES models such as Paluszkiewicz et al. (1994) or the MITgcm used in Johannessen et al. (2013) attempted this finer parametrization which can now be completed with the current dataset. Our results can suggest paths toward better parametrization of convection in models.

4.2. Scalings

The theory developed in Maxworthy and Narimousa (1994) and Marshall and Schott (1999) predicts that the distribution of velocities is symmetrical when there is no impact of rotation and suggests a scaling for the vertical velocities depending on the surface buoyancy losses. The vertical mixing is not influenced by rotation when the convective layer depth limit $h^*=(B/f^3)^{1/2}$ is greater than the convective depth (B being the buoyancy loss, f the Coriolis parameter). Otherwise, Marshall and Schott (1999) predicted that the mixing would not be influenced by Earth's rotation and a symmetrical distribution of velocities in $(Bh)^{1/3}$. In the northwestern Mediterranean, $B=0.2\times10^{-6}$ to 0.5×10^{-6} m^2 s^{-3} which gives $h^*=450$ to 700 m and an associated $w=(Bh^*)^{1/2}=4$ to 7 cm s^{-1}. In the Gulf of Lions, the convection reached the bottom (2,300 m)

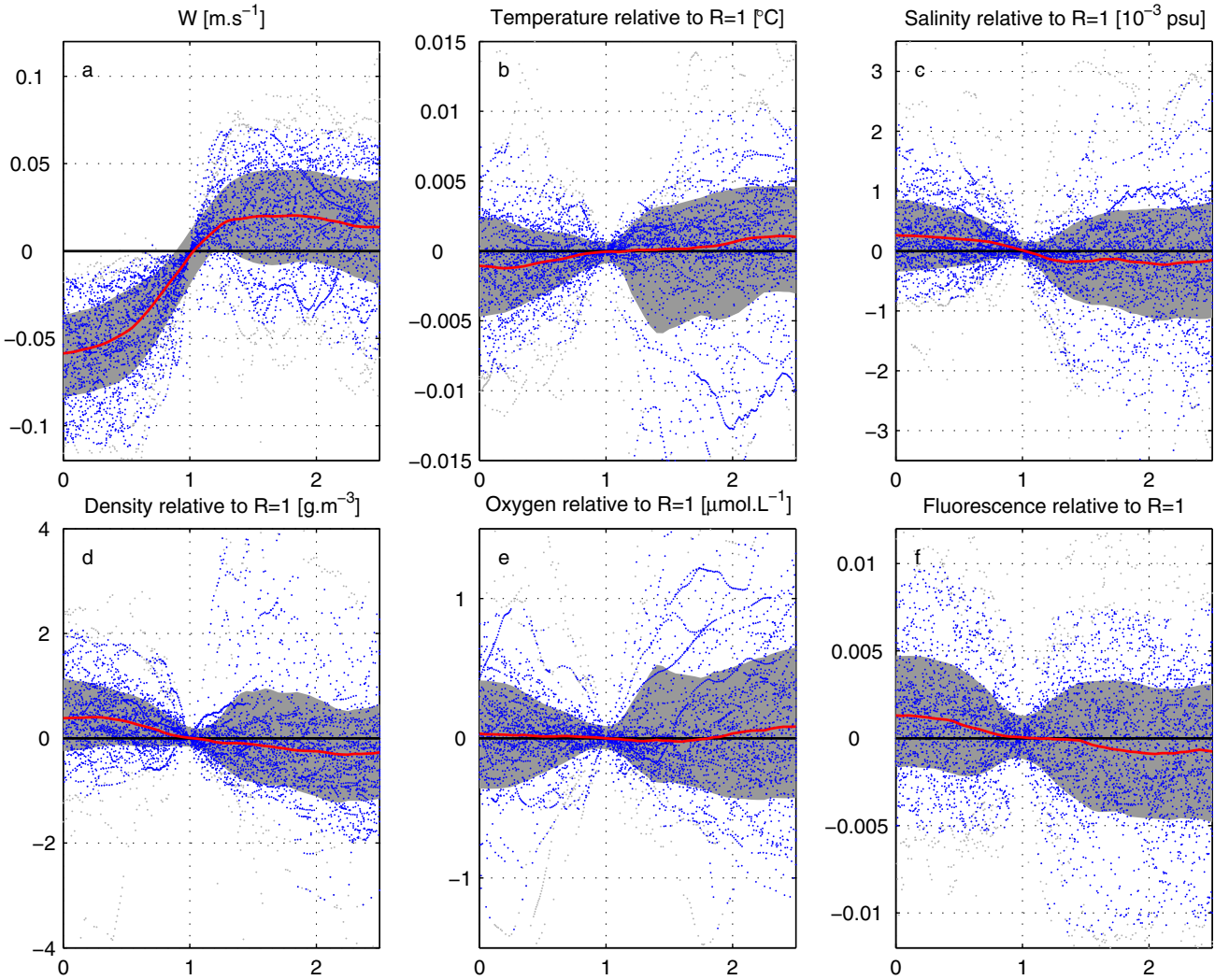

Figure 7. Plume tendencies as detected from two gliders (Campe/ASICSMED and Milou/ASICSMED) during the 2012–2013 winter. The point at R = 1 where the vertical velocities are zero is taken as the reference. The core of the plumes is at R = 0, the environing waters are considered at R = 2.5. The 5% higher and lower values (in gray) are considered outliers. The running standard deviation is in a grey shading and the running mean of the points is within the standard deviation is in red. (a) Water vertical velocity. (b) Temperature relative to R = 1. (c) Salinity relative to R = 1. (d) Density relative to R = 1. (e) Oxygen relative to R = 1. (f) Fluorescence relative to R = 1.

during our episode and we observed velocities up to 18 cm s^{-1}, confirming the influence of rotation on the observed plumes and the asymmetrical velocity distribution in Figure 3. Knowing that the observed convective plumes are under the influence of rotation, we test the scaling suggested by Marshall and Schott (1999). The scaling for the vertical velocities under the influence of rotation is estimated to be in $w=(B_0/f)^{1/2}$. Using the mean value $B_0 = -2.9\times10^{-7}$ m^2 s^{-3} above plumes, we get a vertical velocity of $w = 5.45$ cm s^{-1} in good agreement with what is observed in the plumes.

To complete the study, we suggest a scaling for the variance of w against the buoyancy loss inferred from the heat fluxes. The standard formula for the buoyancy loss gives $B_0 = g\ \frac{\alpha}{C_p}\ \frac{h_{net}}{\rho}$, α being the thermal expansion coefficient of the water, C_p the water heat capacity, h_{net} the net heat flux, and ρ the water density. Using the inferred B_0 and computing the velocity relative to fluxes during the intense episodes (net heat fluxes <-400 W m^{-2}), we consistently obtain a relation in $variance(w)=(B_0/f)^e$ where $e=0.86\pm0.01$ with an RMSE of 0.9992.

4.3. Vertical Diffusion Coefficient

Individual plumes induce intense vertical mixing and we can statistically estimate a vertical diffusion coefficient Kz associated with their overall effect on the water column. We examined in particular two intense

convection episodes (7–9 February and 23–25 February), the second one being represented in Figure 8. Both are characterized by large fluxes and the mixed layer reaching the bottom.

Knowing the size of the plumes, we estimate buoyancy fluctuations b' relative to a 1 h running mean. This is justified by the fact that 1 h represents about 1 km of horizontal glider displacement which is 1.5–2 times the diameter of a plume. The plumes are responsible for a vertical buoyancy flux determined by the correlation of w' and b'. By construction, $<w> = 0$ and thus $w = w'$. Figure 8 shows a $<w'b'> > 0$ tendency demonstrating a statistical buoyancy flux from the surface to the ocean interior. The intense cooling at the surface fits with the $B_0 = 2.9 \times 10^{-7}$ m^2 s^{-3} inferred from the net heat fluxes and is consistent with the increasing of buoyancy flux due to the plumes near the surface. The buoyancy loss then diminishes, its intensity approaching 10^{-7} m^2 s^{-3}. Now looking at the vertical distribution of buoyancy, we observe a mean decrease of buoyancy close to the surface after averaging the buoyancy of the 30 considered profiles. This results from a tendency of densification of the surface layer. The buoyancy distribution was computed relative to the surface, as temporal and spatial variability of the water column can induce lateral gradients of buoyancy. Parametrizing the statistical mean buoyancy flux during the mixing period by a diffusivity flux yields $<w'b'> = -K_z \frac{d<b>}{dz}$ (axis z pointing to the surface). We could thus infer a vertical diffusion coefficient K_z in layers of 50 m (see Figure 8f). After removing outliers caused by too weak or reverse buoyancy gradients between two consecutive layers, we found on average a mean diffusion coefficient of 5.0 ± 3.7 and 7.0 ± 4.3 m^2 s^{-1} for the two mixing events.

This is consistent with the vertical diffusion estimates made by a recent study by Durrieu de Madron et al. (2017, Figure 14) finding 10–50 m^2 s^{-1} to get vertically homogeneous profiles over 28 h for sediment plumes. The mean diffusion coefficient we found is also in good agreement with Klinger et al. (1996) numerical experiments on convective plume dynamics suggesting 10 m^2 s^{-1} for vigorous deep convective events.

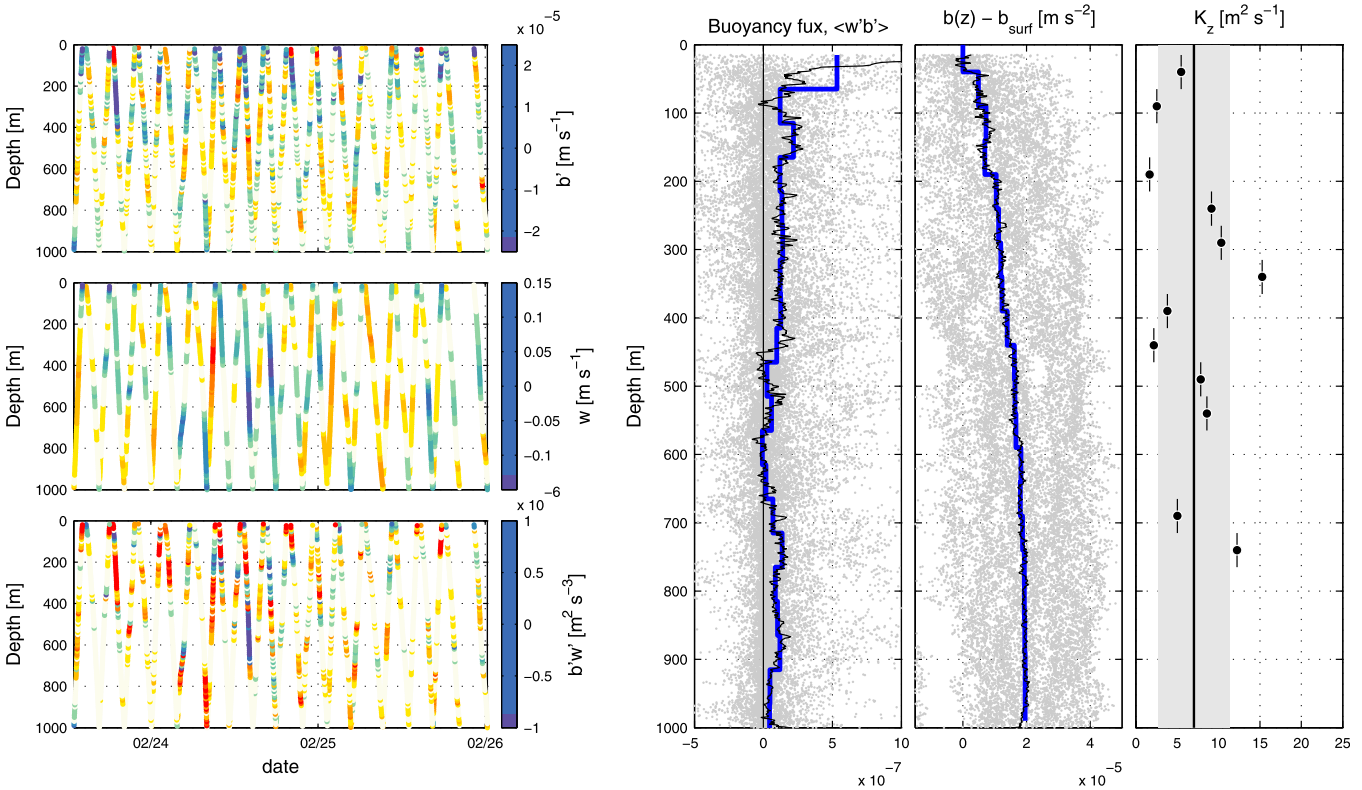

Figure 8. Glider flight conditions and buoyancy losses during a convective period of three days (23–25 February). The left figure shows the along-track buoyancy fluctuations, water vertical velocities, and buoyancy losses. The right figure shows the mean buoyancy fluxes in the water column and its 50 m binned values; the buoyancy relative to the surface and the associated vertical diffusion coefficient. Near-surface data of the top 15 m have been excluded to get rid of spurious data that could have been caused by the rough sea state or cooling of the glider by cooling of the instrument at the surface.

5. Conclusions and Perspectives

Building on the methods presented in Merckelbach et al. (2010) and Frajka-Williams et al. (2011), our study aims at a deeper understanding of the role of convective plumes in the mixing of physical and biogeochemical tracers during deep open-ocean convection events. It provides for the first time a comprehensive characterization of convective plumes on a statistical basis showing an asymmetry between up and down movements with stronger downward velocities. The downward velocities are of higher magnitude than the upward ones (-6 versus $+2$ cm s^{-1} on average). We highlight the relation between these vertical movements and the physical and biogeochemical water properties. Statistically, the plunging waters are colder (-1.8×10^{-3} °C), moderately saltier ($+4.9 \times 10^{-4}$ psu) and thus denser ($+7.5 \times 10^{-4}$ kg m^{-3}) than the surrounding upward ones. The downward waters are also on average a little more fluorescent ($+2.3 \times 10^{-2}$ μg L^{-1}) as phytoplankton is being dragged down. For the first time, the horizontal scales associated with these circulation features are computed from in situ data. The plumes are distant from each other by 2 km on average and have a mean radius of 350 m for their downward component. The newly found properties of the convective plumes as well as their vertical structure is assessed and a description of the convective area is suggested. The plumes get wider and more intense as they get deeper and they cover 27% of the convective area.

The scaling suggested in Marshall and Schott (1999) has been found to be coherent with the observation of the Gulf of Lions plumes under the effect of rotation. A further distribution of the vertical velocity variance is given in $(B_0/f)^{0.86}$. This description could allow for a better parametrization of deep convection in global ocean circulation models as a vertical diffusion coefficient of 7 m^2 s^{-1} has been found to describe the buoyancy losses in the plumes. In atmospheric models, Plant and Craig (2008) suggest a stochastic description of plumes scheme for deep convection, suitable for use in both climate and NWP models. They use a probability distribution function to find plumes which could be inferred from our results as well as their characteristics.

In terms of observations, gliders are not yet able to sample deeper than 1,000 m. The development of gliders able to dive deeper could enable a complete characterization of the plumes by the sampling of their whole vertical extension. The development of new onboard sensors could also allow a further characterization of the physical and biogeochemical properties of the plunging waters. Considering that Durrieu de Madron et al. (2017) use the same glider Campe to compute sediment resuspension in shallower regions, these developments could allow the observation of the plume structure at depth and their interaction with the bottom turbid boundary layer.

Acknowledgments
The hydrographical data were collected and made freely available by the Coriolis project and programs that contribute to it (http://www.coriolis.eu.org). We would like to acknowledge the staff of the National Pool of Gliders of DT-INSU for the sustained gliders deployments. Captains and crew of R/V Le Tethys II (INSU), Le Provence (Phares et Balises), L'Atalante (Ifremer), and Le Suroit (Ifremer), as well as scientists, engineers, and technicians who participated to the MOOSE-GE, HyMeX, DEWEX, and DOWEX different cruises are also warmly thanked. Support was provided by the French MISTRALS program (HyMeX and MERMeX components), the French ANR ASICSMED, the MOOSE long-term observatory (AllEnvi-INSU), and the EU projects FP7 GROOM (grant 284321), FP7 PERSEUS (grant 287600), FP7 JERICO (grant 262584), and the COST Action ES0904 Everyone's Gliding Observatories.

References

Bosse, A. (2015). *Circulation générale et couplage physique-biogéochimie à (sous-) mésoéchelle en Méditerranée Nord-occidentale à partir de données in situ* (Ph.D. thesis). Paris, France: Université Pierre et Marie Curie.

Bosse, A., Testor, P., Houpert, L., Damien, P., Prieur, L., Hayes, D., . . . Mortier, L. (2016). Scales and dynamics of submesoscale coherent vortices formed by deep convection in the northwestern Mediterranean Sea. *Journal of Geophysical Research: Oceans*, *121*, 7716–7742. https://doi.org/10.1002/2016JC012144

Durrieu de Madron, X., Houpert, L., Puig, P., Sanchez-Vidal, A., Testor, P., Bosse, A., . . . Raimbault, P. (2013). Interaction of dense shelf water cascading and open-sea convection in the northwestern Mediterranean during winter 2012. *Geophysical Research Letters*, *40*, 1379–1385.

Durrieu de Madron, X., Ramondenc, S., Berline, L., Houpert, L., Bosse, A., Martini, S., . . . the ANTARES Collaboration. (2017). Deep sediment resuspension and thick nepheloid layer generation by open-ocean convection. *Journal of Geophysical Research: Oceans*, *122*, 2291–2318.

Eriksen, C. C., & Rhines, P. (2008). Convective to gyre-scale dynamics: Seaglider campaigns in the Labrador Sea 2003–2005. In R. R. Dickson, J. Meincke, & P. Rhines (Eds.), *Arctic-subarctic ocean fluxes* (pp. 613–628). Dordecht: Springer. https://doi.org/10.1007/978-1-4020-6774-7_26

Frajka-Williams, E., Eriksen, C. C., Rhines, P. B., & Harcourt, R. R. (2011). Determining vertical water velocities from Seaglider. *Journal of Atmospheric and Oceanic Technology*, *28*, 1641–1656.

Garau, B., Ruiz, S., Zhang, W. G., Pascual, A., Heslop, E. E., Kerfoot, J., & Tintoré, J. (2011). Thermal lag correction on Slocum CTD glider data. *Journal of Atmospheric and Oceanic Technology*, *28*(9), 1065–1071.

Grignon, L., Smeed, D. A., Bryden, H. L., & Schroeder, K. (2010). Importance of the variability of hydrographic preconditioning for deep convection in the Gulf of Lion, NW Mediterranean. *Ocean Science*, *6*(2), 573–586.

Houpert, L., Durrieu de Madron, X., Testor, P., Bosse, A., D'ortenzio, F., Bouin, M., . . . Raimbault, P. (2016). Observations of open-ocean deep convection in the northwestern Mediterranean Sea: Seasonal and interannual variability of mixing and deep water masses for the 2007–2013 period. *Journal of Geophysical Research: Oceans*, *121*, 8139–8171. https://doi.org/10.1002/2016JC011857

Johannessen, O. M., Lygre, K., & Eldevik, T. (2013). *Convective chimneys and plumes in the northern Greenland Sea* (pp. 251–272). Washington, DC: American Geophysical Union. https://doi.org/10.1029/158GM17

Klinger, B. A., Marshall, J., & Send, U. (1996). Representation of convective plumes by vertical adjustment. *Journal of Geophysical Research: Oceans*, *101*(C8), 18175–18182.

Leaman, K. D., & Schott, F. A. (1991). Hydrographic structure of the convection regime in the Gulf of Lions: Winter 1987. *Journal of Physical Oceanography*, *21*(4), 575–598.

Legg, S., & McWilliams, J. C. (2001). Convective modifications of a geostrophic eddy field. *Journal of Physical Oceanography*, *31*, 874–891.

L'Hévéder, B., Mortier, L., Testor, P., & Lekien, F. (2013). A glider network design study for a synoptic view of the oceanic mesoscale variability. *Journal of Atmospheric and Oceanic Technology*, *30*, 1472–1493. https://doi.org/10.1175/JTECH-D-12-00053.1

Madec, G., Chartier, M., Delecluse, P., & Crépon, M. (1991). A three-dimensional numerical study of deep-water formation in the northwestern Mediterranean Sea. *Journal of Physical Oceanography*, *21*, 1349–1371.

Marshall, J., & Schott, F. (1999). Open-ocean convection: Observations, theory, and models. *Reviews of Geophysics*, *37*(1), 1–64.

Maxworthy, T., & Narimousa, S. (1994). Unsteady, turbulent convection into a homogeneous, rotating fluid, with oceanographic applications. *Journal of Physical Oceanography*, *24*(5), 865–887.

MEDOC Group. (1970). Observation of formation of deep water in the Mediterranean Sea, 1969. *Nature*, *225*, 1037–1040. https://doi.org/10.1038/2271037a0

Merckelbach, L., & Smeed, D. (2006). *Simulating gliders*. Paper presented at EGO Conference, Paris.

Merckelbach, L., Smeed, D., & Griffiths, G. (2010). Vertical water velocities from underwater gliders. *Journal of Atmospheric and Oceanic Technology*, *27*(3), 547–563.

Mertens, C., & Schott, F. (1998). Interannual variability of deep-water formation in the northwestern Mediterranean. *Journal of Physical Oceanography*, *28*(7), 1410–1424.

Paluszkiewicz, T., Garwood, R., & Denbo, D. (1994). Deep convective plumes in the ocean. *Oceanography*, *7*(2), 37–44.

Plant, R., & Craig, G. (2008). A stochastic parameterization for deep convection based on equilibrium statistics. *Journal of Atmospheric Sciences*, *65*, 87–105. https://doi.org/10.1175/2007JAS2263.1

Schott, F., Visbeck, M., Send, U., Fischer, J., Stramma, L., & Desaubies, Y. (1996). Observations of deep convection in the Gulf of Lions, northern Mediterranean, during the winter of 1991/92. *Journal of Physical Oceanography*, *26*, 505–524.

Send, U., & Marshall, J. (1995). Integral effects of deep convection. *Journal of Physical Oceanography*, *25*(5), 855–872.

Smeed, D., Merckelbach, L., Griffiths, G., Bryden, H., Grignon, L., Testor, P., & Legg, S. (2007*). Deep ocean convection: Observations from an adaptive network of underwater gliders (doconug)*.

Straneo, F., & Kawase, M. (1999). Comparisons of localized convection due to localized forcing and to preconditioning. *Journal of Physical Oceanography*, *29*(1996), 55–68.

Testor, P., Durrieu de Madron, X., Mortier, L., D'ortenzio, F., Legoff, H., Dausse, D., . . . Houpert, L. (2016). LION observatory data. SEANOE. https://doi.org/10.17882/44411

Testor, P., & Gascard, J.-C. C. (2006). Post-convection spreading phase in the northwestern Mediterranean Sea. *Deep Sea Research Part I: Oceanographic Research Papers*, *53*(5), 869–893.

Testor, P., Houpert, A. B., Margirier, L., D'ortenzio, F., Mortier, F., Legoff, L., . . . Ribotti, A. (2017). Multi-scale observations of deep convection in the northwestern Mediterranean Sea during winter 2012–2013 from a multi-platform approach. *Journal of Geophysical Research: Oceans*. https://doi.org/10.1002/2016JC012671.

Visbeck, M., Marshall, J., & Jones, H. (1996). Dynamics of isolated convective regions in the ocean. *Journal of Physical Oceanography*, *26*, 1721–1734. https://doi.org/10.1175/1520-0485(1996)026<1721:DOICRI>2.0.CO;2